

An advanced 3D boundary element method for characterizations of composite materials

X.L. Chen^a, Y.J. Liu^{b,*}

^aMechanical Engineering Program, School of Engineering and Computer Science, Washington State University Vancouver, Vancouver, WA 98686, USA

^bDepartment of Mechanical, Industrial and Nuclear Engineering, University of Cincinnati, P.O. Box 210072, Cincinnati, OH 45221-0072, USA

Received 30 September 2004; revised 29 December 2004; accepted 30 December 2004

Available online 8 April 2005

Abstract

Some recent developments in the modeling of composite materials using the boundary element method (BEM) are presented in this paper. The boundary integral equation for 3D multi-domain elasticity problems is reviewed. Difficulties in dealing with nearly-singular integrals, which arise in the BEM modeling of composite materials with closely packed fillers or of thin films, are discussed. New and improved techniques to deal with the nearly-singular integrals in the 3D elasticity BEM are presented. Numerical examples of layered thin films and composites with randomly distributed particles and fibers are studied. The advantages and limitations of the BEM approach in modeling advanced composites are also discussed. The developed BEM with multi-domain and thin-body capabilities is demonstrated to be a promising tool for simulations and characterization of various composite materials.

© 2005 Elsevier Ltd. All rights reserved.

Keywords: Boundary element method; Composite materials; Nearly-singular integrals

1. Introduction

Composites have been studied for decades. The anisotropic nature and the configurations in which they are fabricated allow for better design of structures with tailored material properties to meet demanding conditions. Two major categories of composites are available, namely the reinforced composites and the structural composites. Reinforced composites have been ideal material candidates for defense, aerospace and consumer goods industries. Especially, the discontinuously reinforced composites with short fibers or particles are popular since they can be molded into arbitrary shapes by conventional manufacturing techniques [1–3]. Structural composites, traditionally used in aircraft structures, have found recent applications in semiconductor devices and microtransducer systems. Innovations in thin-film deposition techniques result in desirable film qualities and cost-effective volume production of thin films [4–6]. This leads to strong interest in utilizing thin

films type of structural composites for the state-of-art applications at the macro and micro-scales. With numerous potential applications, composites are attracting more and more research attentions and their performance are constantly improved to meet the growing challenges.

Characterization of composites thus becomes increasingly important. It is a critical step in understanding new materials before they can be used to build structures. With the increasing complexity in composites being developed, new characterization tools are needed that can analyze, for example, complicated load transfer mechanisms or stress distributions in composite materials. Characterization based on computer simulations has gained increasing interests. Through a representative volume element (RVE), a statistically representative microstructure of a composite, effective material constants can be extracted based on a constitutive model and some well-designed simulations. The advantages of the simulation-based characterization are obvious. For example, it can save the experimental efforts and costs by simply using computer programs to perform repetitive studies.

Numerical methods, primarily the finite element method (FEM) and the boundary element method (BEM), have been used in structural simulation and characterization of

* Corresponding author. Tel.: +1 513 556 4607; fax: +1 513 556 3390.
E-mail address: yijun.liu@uc.edu (Y.J. Liu).

composite materials for several decades. In the early FEM studies, random microstructures in reinforced composites are simplified into periodic spatial arrangement of inclusions by enforcing periodic boundary conditions. For example, in Refs. [7–9], RVEs with multiple inclusions are studied using the FEM. It is shown in Ref. [8] that FEM simulations are performed on sliced thin portions of random microstructure RVE models due to computational limitations. Refs. [10,11] give some 3D FEM examples of thin films or thin laminated composites. Extremely dense meshes are created near thin material regions involved in these studies, requiring intensive computation. Generally speaking, the domain-based FEM faces many challenges in material simulation. Composite materials often contain arbitrarily thin regions or randomly dispersed inclusions of different size and shapes, yet FEM imposes strict requirement on the element quality such as aspect ratios, skewness and so on in order to ensure the solution accuracy. In order to describe the detailed configuration as well as to have smooth transition at interfaces among different materials, FEM requires extremely fine meshes near these regions, resulting in a large computational model to solve.

It has been shown that the BEM has many distinctive advantages over the FEM for modeling many material related problems [12–19], regarding, e.g. the mesh generation, treatment of thin regions, and accuracy. Among the challenges for the BEM are the issues of singular and nearly-singular integrals, possible domain discretization in nonlinear analysis, and the solution efficiency. However, considerable progresses in these areas have been made for the BEM in recent years. The day when the computational advantages of the BEM over some domain based methods in some applications become too attractive for end users to ignore may not be far away [20].

In this paper, an advanced multi-domain BEM with thin-body capabilities is presented for 3D analyses of various composite materials based on the elasticity theory. Related issues to the BEM in these applications, such as nearly-singular integrals, which are crucial to the successful applications of the BEM to thin shapes, are discussed. Numerical examples using the BEM, including thin films, short-fiber and particle reinforced composites, are presented to demonstrate the effectiveness and potential of the developed 3D multi-domain BEM in modeling and characterization of composite materials.

2. Boundary integral equation formulation and nearly-singular integrals

Composite materials are inhomogeneous and anisotropic in nature, although their constituents, such as the matrix and fibers, can be considered homogeneous, isotropic and linearly elastic. Based on these assumptions and at the constituent level, the following conventional boundary integral equation (BIE) for 3D elastostatic problems can

be applied

$$\int_S T_{ij}^{(\beta)}(P, P_0)[u_j^{(\beta)}(P) - u_j^{(\beta)}(P_0)]dS(P) = \int_S U_{ij}^{(\beta)}(P, P_0)t_j^{(\beta)}(P)dS(P), \quad \forall P_0 \in S, \quad (1)$$

in which superscript β denotes any single domain of n domains; $u_i^{(\beta)}$ and $t_i^{(\beta)}$ are the displacement and traction fields in that domain, respectively; $U_{ij}^{(\beta)}(P, P_0)$ and $T_{ij}^{(\beta)}(P, P_0)$ the displacement and traction kernels (Kelvin's solution); P the field point (integration point); P_0 the source point (collocation point); and S the domain boundary. BIE (1) is in a weakly-singular form of the conventional BIE and does not involve computations of any singular integrals in the discretization [21,22].

BIE (1) can be applied safely for materials of complex configuration, as long as the nearly-singular integrals, which occurs when the source point P_0 is close to (e.g. the distance to element length ratio is less than 0.1) but not on the surface of integration, can be computed accurately and efficiently. In modeling composite materials, the nearly-singular integrals arise quite often due to the many thin regions present. They must be dealt with accurately to avoid any degradation of simulation results. Earlier efforts for both 3D and 2D BEM have resulted in significant improvements in the accuracy of evaluating nearly-singular integrals. Details of how to handle the nearly-singular integrals in the BEM can be found in Refs. [17,23–29]. Among these research work, the line integral approach [17,27,28] is found to be very efficient. The main idea of this approach is to avoid evaluating the nearly-singular integrals numerically. Instead, the integrals are transformed into line integrals to be evaluated on the contour boundary of a surface element for 3D cases [27,28], or into direct function evaluations for 2D cases [17].

In the line integral approach [27,28], the integral with the traction kernel function in BIE (1) is treated as follows

$$\int_{\Delta S} T_{ij}(P, P_0)u_j(P)dS(P) = \int_{\Delta S} T_{ij}(P, P_0)[u_j(P) - u_j(P'_0)]dS(P) + u_j(P'_0) \int_{\Delta S} T_{ij}(P, P_0)dS(P), \quad (2)$$

where P'_0 (an image point) is the projection of P_0 (source point) on ΔS (a surface element, see Fig. 1).

The essence of the above treatment is that the last term in Eq. (2) can then be transformed into line integrals using the Stokes' theorem and properties of the solid angle integral (see details in Ref. [28]), and that the remaining term in the right-hand side of the equation is at most nearly-weakly-singular. To explain further, consider a polar coordinate transformation $dS = r' dr' d\theta$, where $r' = |PP'_0|$ and $r = |PP_0|$ (Fig. 1). The integral on the left-hand side of

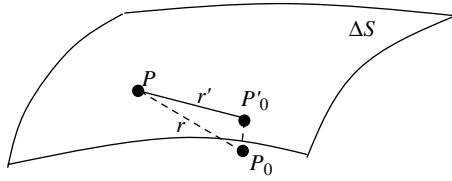


Fig. 1. Source point P_0 near the surface ΔS of integration.

Eq. (2) is of $O(r'/r^2)$. Such integrals become nearly-singular as P approaches P'_0 when P_0 is near ΔS , which is often the case we will encounter in BEM simulation involving thin shapes. However, owing to the fact that $u_j(P) - u_j(P'_0)$ is of $O(r')$ from Taylor expansion, the first integral on the right hand side of (2) is now reduced to the order of $O(r'^2/r^2)$, which is at most nearly-weakly-singular as $r' \rightarrow 0$ and $r \rightarrow |P_0 P'_0|$. Similarly, we notice that the order of integral $\int_{\Delta S} U_{ij}(P, P_0) t_j(P) dS(P)$ in BIE (1) is $O(r'/r)$, which is also nearly-weakly-singular in the worst-case scenario. These nearly-weakly-singular integrals can introduce significant errors when they are evaluated using standard quadrature rules, although these errors are in general smaller than those produced by the nearly-singular integrals in the BEM.

The line integral approach has been proved successful for many BEM material/structure simulation involving thin shapes. Satisfactory results were obtained using this approach when the distance (between the source point and the surface of integration) to element length ratio is around 0.01 for 3D cases [28] and below 1×10^{-6} for 2D cases [17].

However, to tackle more challenging modeling tasks, improvements in the line integral approach are needed to further regularize the still existing nearly-weakly-singular integrals, which were not treated in the previous works reported in Refs. [27,28] for 3D problems. In this paper, an improved method with better treatment of nearly-weakly-singular integrals for 3D elastostatic problems is presented and its effectiveness is demonstrated by using examples with the distance to element length ratio as small as 1×10^{-6} . In this improved approach for 3D cases, a nonlinear coordinate transformation is applied on the element of integration with the source point near by, in combination with the original line integral approach [27,28]. With this improved approach, composite materials involving arbitrary thin shapes can be modeled and characterized more accurately with much coarser BEM meshes. In the following, related regularization techniques for better treatment of nearly-weakly-singular integrals in 3D BEM are reported.

3. New treatment of the nearly-weakly-singular integrals for 3D BEM

When arbitrary thin shape region is involved in BEM material simulation, accurate evaluation of the resulting nearly-weakly-singular integrals remains a challenge.

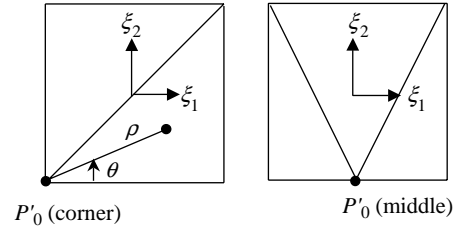


Fig. 2. Subdivision for surface elements in the intrinsic coordinate system.

In order to further improve the accuracy in the evaluation of these integrals, an efficient regularization technique is presented here. A simple nonlinear-coordinate transformation, which has been employed in the 2D BEM implementation [17], is applied in the 3D BEM to further ‘regularize’ the nearly-weakly-singular integrals. Details of the implementations can be found in Ref. [30].

To briefly describe the problem, let us denote $T_{ij}(P, P_0) [u_j(P) - u_j(P'_0)]$ as F and reexamine Eq. (2). Note that in order to make use of the polar coordinate transformation, a square element in the intrinsic coordinate system can be divided into two or three triangular subdivisions, depending on where the image point P'_0 is located (corner or middle node) (Fig. 2). Hence, the nearly-weakly-singular term (the first term on the right-hand side of Eq. (2)) can be expressed as

$$\int_{\Delta S} F dS = \int_{-1}^1 \int_{-1}^1 F(\xi_1, \xi_2) J_1(\xi_1, \xi_2) d\xi_1 d\xi_2 = \sum_{l=1}^{2 \text{ or } 3} \int_{\theta_b^l}^{\theta_b^l + \Delta\theta^l} \int_0^{\Delta\rho^l} F(\rho, \theta) J_1(\rho, \theta) \rho d\rho d\theta, \quad (3)$$

where J_1 is the Jacobian of transformation from dS to $d\xi_1 d\xi_2$; $\Delta\rho$ the line segment connecting the pole and the Gaussian points in a subdivision; θ_b the starting angle of integration and $\Delta\theta$ the subdivision angle at the pole, respectively (Fig. 3). Superscript l in $\Delta\rho$, θ_b and $\Delta\theta$ indicates the l th subdivision.

To use Gaussian quadrature, the following transformation is applied to map a triangular subdivision in Eq. (3) into a standard square (superscript l is omitted for simplicity)

$$d\rho = \frac{\Delta\rho}{2} d\eta_1 \quad \text{and} \quad d\theta = \frac{\Delta\theta}{2} d\eta_2, \quad (4)$$

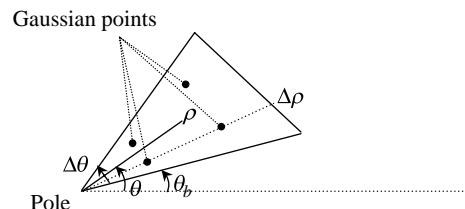


Fig. 3. A triangular subdivision in the polar coordinate system.

where η_1 and η_2 represent the new coordinates for the mapped square.

Substituting Eq. (4) into (3) gives

$$\int_{\Delta S} F \, dS = \sum_{l=1}^{2 \text{ or } 3} \int_{-1}^1 \int_{-1}^1 G(\eta_1, \eta_2) J_1(\eta_1, \eta_2) J_2(\eta_1, \eta_2) d\eta_1 d\eta_2, \quad (5)$$

where $G = F\rho$ and

$$J_2 = \begin{vmatrix} \frac{\partial \rho}{\partial \eta_1} & \frac{\partial \rho}{\partial \eta_2} \\ \frac{\partial \theta}{\partial \eta_1} & \frac{\partial \theta}{\partial \eta_2} \end{vmatrix}.$$

Introducing the following nonlinear coordinate transformation

$$\zeta_1^m = \frac{1}{2}(\eta_1 + 1) \quad \text{or} \quad \eta_1 = 2\zeta_1^m - 1, \quad (6)$$

with m being the order of nonlinearity for the coordinate transformation, Eq. (5) becomes:

$$\begin{aligned} \int_{\Delta S} F \, dS &= \sum_{l=1}^{2 \text{ or } 3} \int_{-1}^1 \int_0^1 G(\zeta_1, \zeta_2) J_1(\zeta_1, \zeta_2) J_2(\zeta_1, \zeta_2) 2m\zeta_1^{m-1} d\zeta_1 d\zeta_2, \end{aligned} \quad (7)$$

Adjusting the interval of integration for ζ_1 from $[0, 1]$ to $[-1, 1]$, it finally gives:

$$\begin{aligned} \int_{\Delta S} F(\rho, \theta) dS &= \sum_{l=1}^{2 \text{ or } 3} \int_{-1}^1 \int_{-1}^1 G(\zeta_1, \zeta_2) J_1(\zeta_1, \zeta_2) J_2(\zeta_1, \zeta_2) m \\ &\times \left(\frac{\zeta_1 + 1}{2} \right)^{m-1} d\zeta_1 d\zeta_2. \end{aligned} \quad (8)$$

Through the above transformations, a somewhat uniform distribution of Gaussian points in the radial direction becomes non-uniform, with more points being shifted towards the pole. This allows for greatly improved accuracy in the evaluation of nearly-weakly-singular integrals using the ordinary quadrature. Fig. 4 clearly shows the regularization effect of integrand when $|P'_0 P_0| = 10^{-5}$. The drastic change of the irregular integrand near the coordinate origin is smoothed out after the new transformation. It is also shown in Fig. 4 that a higher-order nonlinear transformation provides better regularization effect.

Very good results have been obtained using this improved line integral approach, in which the distance to element length ratio can further go down to 1×10^{-6} in 3D examples. This is sufficient to deal with any thin domains in the simulation of material problems efficiently without having to use many smaller elements. A multi-domain BEM code, which can handle thin shapes and a large number of domains, has been developed based on this approach for the study of composite materials. The details of the BEM

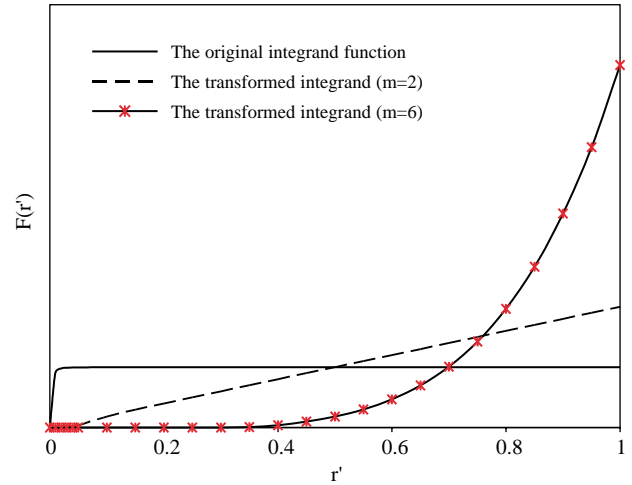


Fig. 4. The integrands before and after the nonlinear coordinate transformation.

implementation can be found in Ref. [30]. Preliminary studies of thin films and fiber and particle-reinforced composites using the developed 3D multi-domain BEM code have been carried out. Next, the formulas for extracting the effective material constants of reinforced composites are reviewed, before the numerical results are reported in Section 5.

4. Formulas for extracting the effective material constants

For completeness, some formulas for extracting the effective material constants for a fiber-reinforced composites are listed in this section. Complete derivations of these formulas can be obtained by referring to Refs. [31,32].

The simulation-based material characterization is achieved through the assumption of a constitutive model that correctly describes the stress–strain relations of a composite. For reinforced composites such as aligned fiber or particle reinforced composites, a transversely isotropic constitutive model can be safely employed. A transversely isotropic material has the simplest form of anisotropy, where the transverse plane is assumed to be the plane of isotropy. This reduces the number of independent elastic constants to five (Young's moduli E_x and E_z , Poisson's ratios ν_{xy} and ν_{zx} , and shear modulus G_{xz} , with z in the direction of the fibers). To characterize a composite, consider a *homogenized* elastic material model corresponding to the representative volume element of the composite sample. This homogenized elastic model is filled with a single, *transversely isotropic* material with the five effective material constants to be determined. The general 3D stress–strain relation relating the normal stresses ($\sigma_x, \sigma_y, \sigma_z$) and strains ($\varepsilon_x, \varepsilon_y, \varepsilon_z$) for a *transversely isotropic* material are

as follows [31]:

$$\begin{Bmatrix} \varepsilon_x \\ \varepsilon_y \\ \varepsilon_z \end{Bmatrix} = \begin{bmatrix} \frac{1}{E_x} & -\frac{\nu_{xy}}{E_x} & -\frac{\nu_{zx}}{E_z} \\ -\frac{\nu_{xy}}{E_x} & \frac{1}{E_x} & -\frac{\nu_{zx}}{E_z} \\ -\frac{\nu_{zx}}{E_z} & -\frac{\nu_{zx}}{E_z} & \frac{1}{E_z} \end{bmatrix} \begin{Bmatrix} \sigma_x \\ \sigma_y \\ \sigma_z \end{Bmatrix} \quad (9)$$

Consider the dimensions of the RVE to be of length L (in the z -direction) and cross-sectional area $2a \times 2a$ (in the x - and y -directions). Three loading cases can be devised to provide five equations based on the elasticity theory to determine the five unknown constants (Young’s moduli E_x and E_z , Poisson’s ratios ν_{xy} and ν_{zx} , and shear modulus G_{xz}), as in Ref. [32]. For example, to determine the longitudinal Young’s modulus E_z , the RVE is stretched by ΔL in the z -direction to provide

$$E_z = \frac{\sigma_{ave}}{\varepsilon_z} = \frac{L}{\Delta L} \sigma_{ave}, \quad (10)$$

where L is the length of the RVE in the z -direction, A the cross-sectional area of the RVE, and σ_{ave} the averaged stress in the z -direction which can be calculated from the BEM results by:

$$\sigma_{ave} = \frac{1}{A} \int_A \sigma_z(x, y, L/2) dx dy. \quad (11)$$

With the same loading condition, one obtains an expression for the Poisson’s ratio

$$\nu_{zx} = -\left(\frac{\Delta a}{a}\right) / \left(\frac{\Delta L}{L}\right), \quad (12)$$

in which, Δa is the change in a when the RVE is stretched in the z -direction.

Now, consider another loading case with a pressure load p on the two lateral surfaces normal to y -direction and displacement constraint in z -direction on both ends of the RVE, one obtains [32]:

$$E_x = E_y = \frac{1}{\frac{\Delta y}{pa} + \frac{\nu_{zx}^2}{E_z}}, \quad (13)$$

$$\nu_{xy} = -\left(\frac{\Delta x}{pa} + \frac{\nu_{zx}^2}{E_z}\right) / \left(\frac{\Delta y}{pa} + \frac{\nu_{zx}^2}{E_z}\right), \quad (14)$$

where Δx (<0) and Δy (>0) are the changes of dimensions in the x - and y -direction, respectively, in this load case. Another simple torsion loading case can be employed to determine the last effective constant G_{xz} . Examples in characterizing composites using the developed BEM and the above-mentioned formulas for both aligned short fiber and particle reinforced composites are given in Section 5.

5. Numerical results

Numerical results for the study of composite materials based on the developed 3D multi-domain BEM simulation are presented in this section. Examples of thin films/coatings and reinforced composite with randomly distributed short fibers or particles are given to demonstrate the efficiency and accuracy of the developed BEM in material characterization. Surface quadratic triangular and quadrilateral elements are used in this study.

5.1. Thin films and coatings

The developed BEM is first tested on a single-layer thin film to demonstrate its capability in handling thin shapes (Fig. 5). Fig. 6 shows a test on the computation of nearly-singular integrals in BIE (1) using the new improved approach. A thin film of dimension $L \times L \times h$ is roller-supported (constrained in the normal direction) on the bottom and loaded with the normal traction on the top (Fig. 5). The results in Fig. 6 show the lateral displacements at a corner point, for which the analytical solution can be found readily. It is shown that the BEM results for the displacements deteriorate and eventually go out of the range of the plot if the nearly-singular integrals are not computed with any special schemes as the thickness h is decreased (Regular BEM, Fig. 6). However, results can stay with

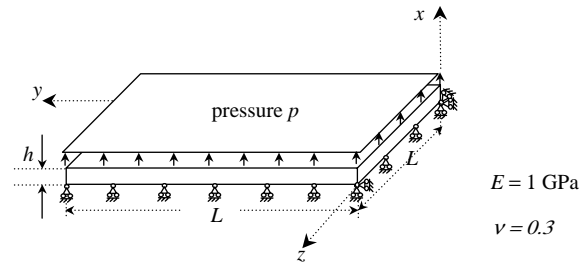


Fig. 5. A thin film structure under a pressure load p .

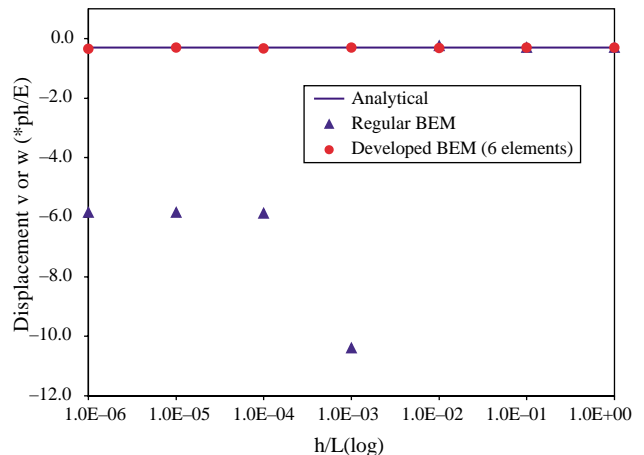


Fig. 6. Lateral displacement v or w at corner point (h, L, L).

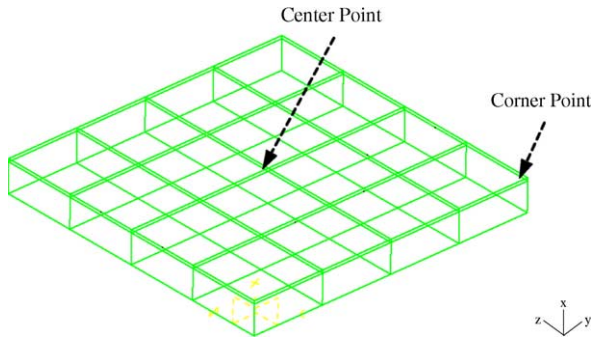


Fig. 7. BEM mesh for a double-layer thin film.

the analytical solution even as the thickness ratio is reduced to 1×10^{-6} if the new approach is used for computing the nearly-singular integrals (Developed BEM, Fig. 6). Notice that only six elements are used in this case, one on each surface of the thin film (plate). This example demonstrates that the developed 3D BEM code can handle nearly-singular integrals very accurately, without the need to increase the number of elements in an analysis. This will be very beneficial for the modeling of composite materials, for which any reduction of the number of elements will help improve the efficiency of the modeling. This example also suggests that the so called *needle-like elements* on the edges do not pose any problem to the BEM, once the nearly-singular integrals are completely removed.

Next, the accuracy in multi-domain applications of the developed BEM is verified through a layered thin film example. A double-layered thin film, with dimension $1 \times 1 \times 0.01 \text{ m}^3$ for the upper layer and $1 \times 1 \times 0.1 \text{ m}^3$ for the lower layer, is loaded similarly as in the previous example. The BEM mesh is shown in Fig. 7, with needle-like elements (element aspect ratio equal to 25:1) being used. This type of needle elements needs to be avoided in regular BEM implementations. The same material ($E = 1 \text{ GPa}$, $\nu = 0.3$) is used for both layers in order to avoid stress singularity issues. Fig. 8 shows the deformation results

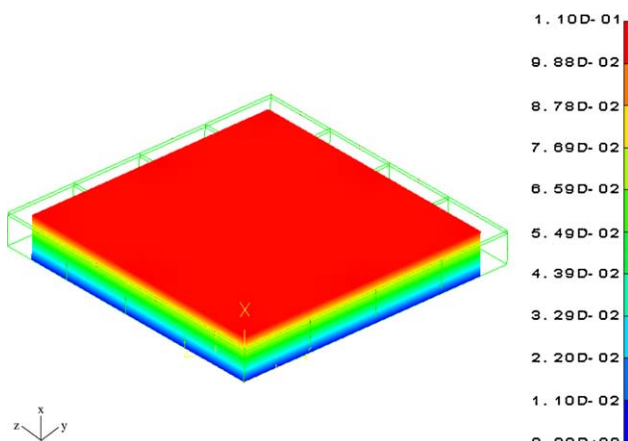


Fig. 8. Vertical deformation of the double-layer thin film from BEM.

Table 1

Comparison of stress values (in the thickness direction) at center and corner locations on the top surface between the BEM and analytical solutions

Normal stress in thickness direction	BEM (GPa)	Analytical (GPa)
At center point	1.0	1.0
At corner point	0.966	1.0

obtained from the developed BEM, which is exactly the same as the analytical prediction. Comparisons are also made for stress values in the thickness direction at two different locations on the top surface between the BEM and analytical solutions (Table 1). The stress values obtained have the largest error of 3% compared with the analytical solution, even with the presence of needle elements in the mesh.

Finally, a double-layered spherical shell with a hollow steel inner layer and titanium coating under external pressure is studied, for which the analytical solution is provided in Appendix. The boundary condition is applied so that the spherical shell is free to contract/expand without any rigid body motion or extra-constraints. For simplicity, the inner radius of the steel shell is given as 1.0 m; the pressure is 1.0 GPa; and both layers are assumed to have the same thickness. Material properties are: $E_A = 110 \text{ GPa}$, $\nu_A = 0.34$ for titanium and $E_B = 200 \text{ GPa}$, $\nu_B = 0.3$ for steel. A BEM mesh is given in Fig. 9. The radial displacement values at the interface from the BEM and analytical solution (see Appendix) are plotted in Fig. 10. The BEM solution with $m = 6$ accurately describes the rapid change of the radial displacement as the coating thickness varies from 10^{-2} to 10^{-4} m . The above examples successfully demonstrate the capabilities of the developed multi-domain 3D BEM in thin film and coating applications.

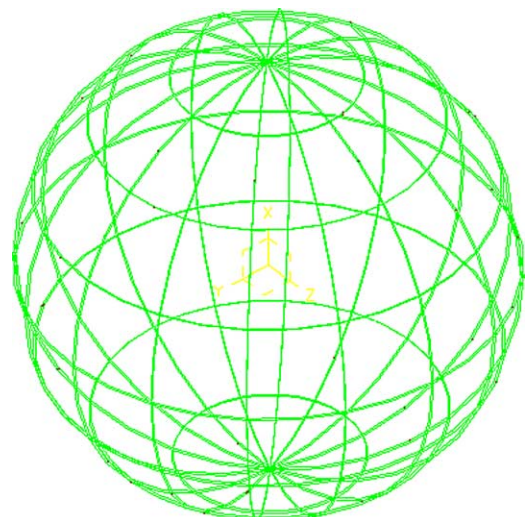


Fig. 9. BEM mesh for a coated spherical shell.

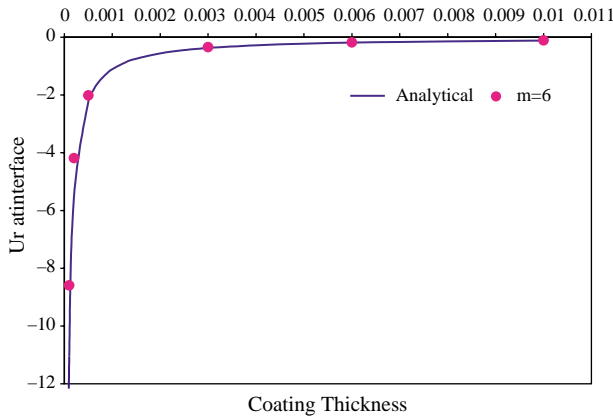


Fig. 10. Radial displacement at the interface for the coated spherical shell.

5.2. Short-fiber-reinforced composites and particle-reinforced composites

Numerical studies for 3D RVEs with randomly distributed, but aligned (for short fibers), inclusions are presented in this section using the developed multi-domain BEM. Due to the complex configurations and arbitrarily close distances between inclusions, such models cannot be analyzed by regular BEM without using a large number of elements. However, very coarse meshes can be used with the improved BEM to study such problems.

A square RVE with 12 randomly distributed, yet aligned, short fibers is studied first. A polymer material with $E_m = 4.6$ GPa and $\nu_m = 0.36$ is used for the matrix; and aluminum alloy with $E_f = 4.6$ GPa and $\nu_f = 0.3$ for the fibers. The RVEs are roller supported on one end and applied with a uniform normal displacement ($\Delta L = 1.0$) on the other end. The side surfaces are allowed for free expansion or contraction. Fig. 11 shows the BEM mesh. Converged BEM results of the total displacement, maximum principal stress and maximum shear stress are shown in Figs. 12–14, respectively. The advantage of the BEM in the meshing step is obvious, with very coarse surface mesh built for the boundaries and interfaces. The stresses in the matrix are

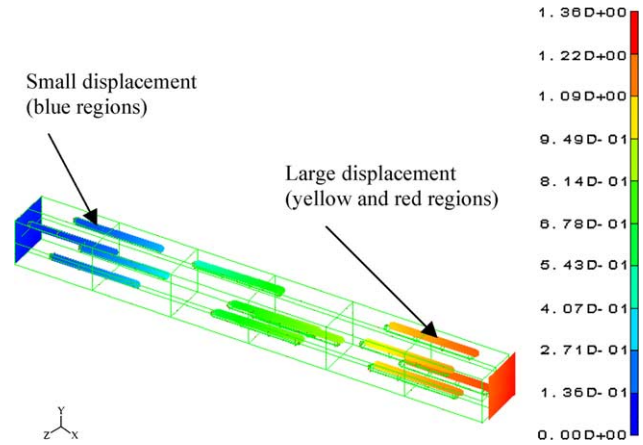


Fig. 12. Total displacement plot from BEM results.

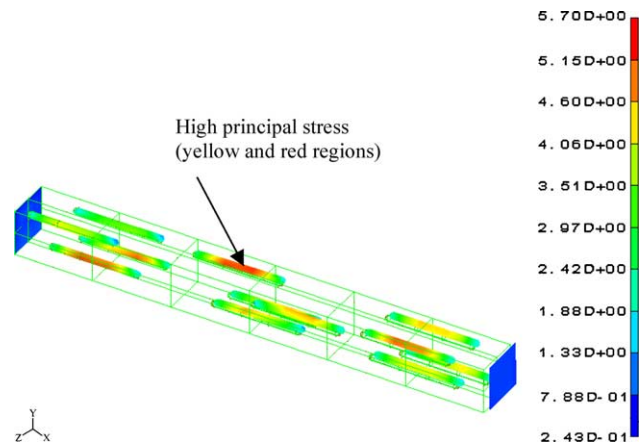


Fig. 13. Maximum principal stress plot from BEM results.

significantly lower than the stresses in the fibers. This predicts that the fibers carry most of the load in the material sample, which is expected since fibers are much stiffer than the matrix material. The results also show the interfacial load transfer mechanism that the load is transferred from the matrix to the fibers through the interfacial shear stress. Similar simulation is performed on a square RVE with

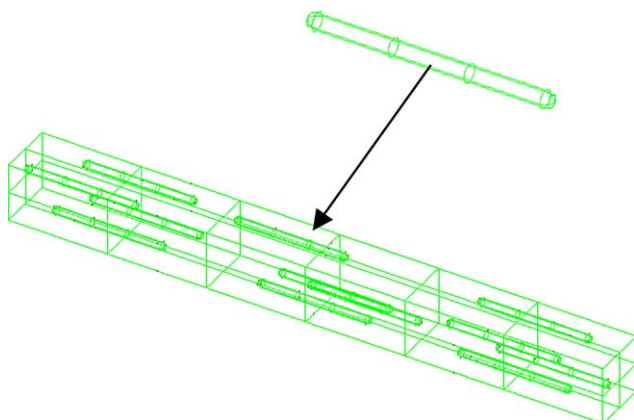


Fig. 11. BEM mesh for the short-fiber reinforced composite.

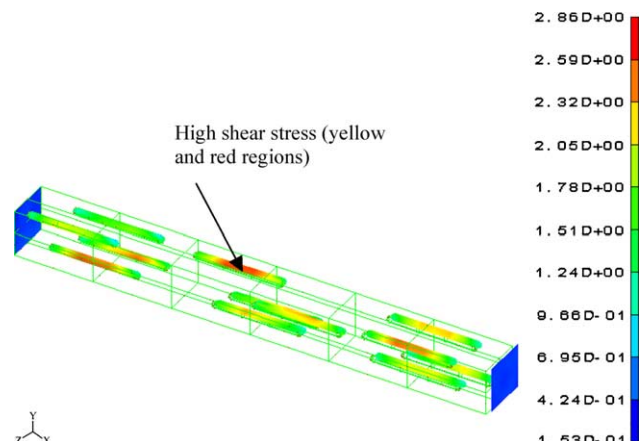


Fig. 14. Maximum shear stress plot from BEM results.

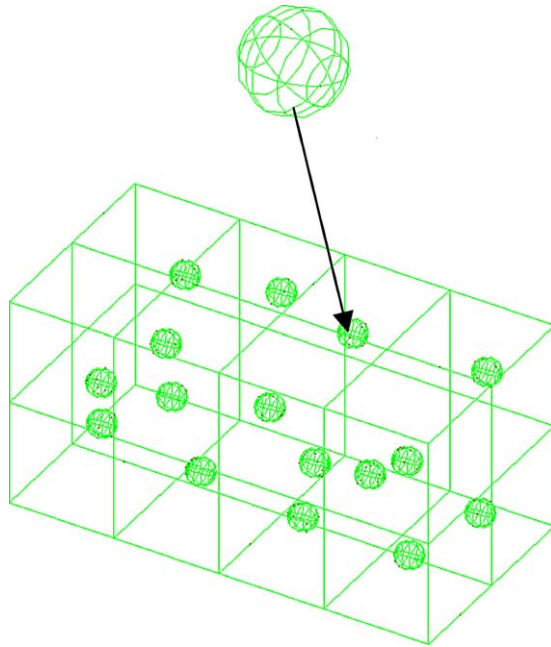


Fig. 15. BEM mesh for the particle-reinforced composite.

16 randomly distributed spherical particles. BEM mesh, converged total displacement, maximum principal stress and maximum shear stress are shown in Figs. 15–18, respectively.

Effective material properties can be readily extracted from these BEM simulations. Given an RVE dimension of $10.5 \times 1 \times 1 \text{ m}^3$ for the short fiber composite and $3.2 \times 1.6 \times 1.6 \text{ m}^3$ for the particle composite, our computed average stresses σ_{ave} from the BEM results are 0.57 and 1.39 GPa, respectively. Plugging these values (including $\Delta L=1.0$) into Eq. (10), the effective longitudinal Young's moduli from BEM results are $E_z=6.0 \text{ GPa}$ for the short fiber composite and $E_z=4.5 \text{ GPa}$ for the particle composite, respectively.

The above characterization results are compared with other theoretical predictions such as the Halpin–Tsai estimation [33] for further verification (see Table 2).

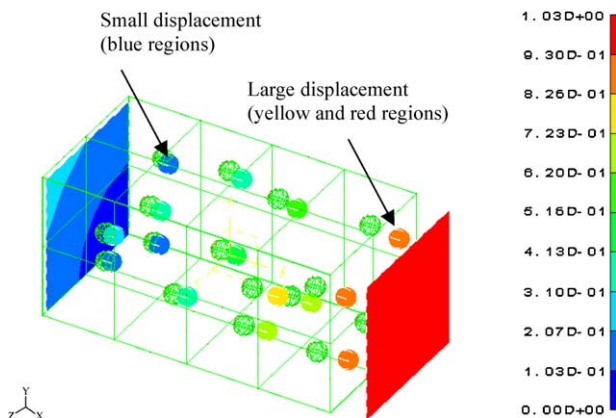


Fig. 16. Total displacement plot from BEM results.

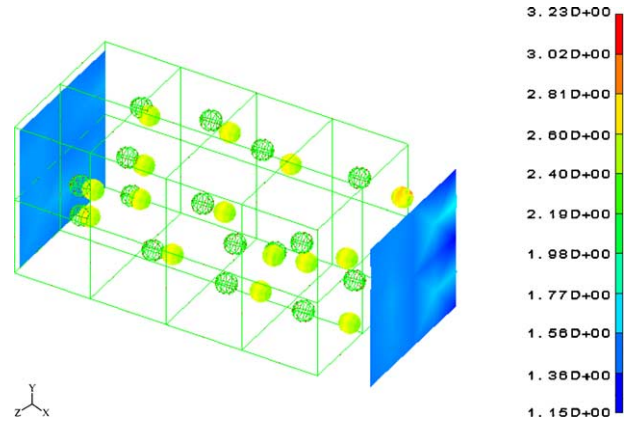


Fig. 17. Maximum principal stress plot from BEM results.

The empirical Halpin–Tsai equation gives $E_z = E_m((1 + \xi\eta\phi)/(1 - \eta\phi))$. Here ξ is the inclusion aspect ratio ($=l/r$, with l being the length and r the radius of the inclusions); η is a constant ($\eta = (\alpha - 1)/(\alpha + \xi)$) and $\alpha = E_f/E_m$; E_m, E_f the Young's moduli of the matrix and inclusion materials, respectively; and ϕ the volume fraction of the inclusions. For our short fiber-reinforced composite model with a 4% fiber volume fraction, the Halpin–Tsai equation gives an estimate of $E_z=6.2 \text{ GPa}$. Similarly, for the particle-reinforced composite model with a 0.8% volume fraction, the Halpin–Tsai equation estimates $E_z=4.7 \text{ GPa}$.

From the above comparisons, we see that the Halpin–Tsai estimations are very close to our BEM calculated effective longitudinal Young's moduli. Both Halpin–Tsai and the BEM calculations predict a 30% increase in the longitudinal modulus of the aluminum short-fiber polymer matrix composite if short fibers are dispersed in an aligned random manner at a volume fraction of 4%. Both also estimate that by randomly adding aluminum particles at a volume fraction of 0.8%, there is negligible impact on the longitudinal modulus of the polymer matrix composite. These results show that the BEM-based material characterizations are efficient and effective. Similar studies can be performed for composites with different compositions and configurations. They can also be readily extended to

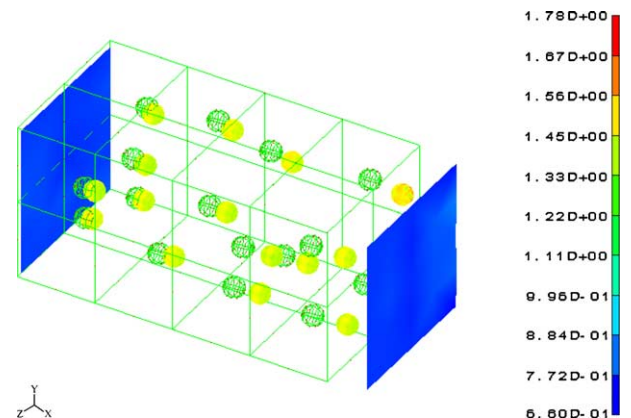


Fig. 18. Maximum shear stress plot from BEM results.

Table 2

Comparison of the effective longitudinal Young's moduli between the BEM-based characterization and the Halpin–Tsai estimation

	BEM (GPa)	Halpin–Tsai (GPa)
Short-fiber composite (4% fiber volume fraction)	6.0	6.2
Particle composite (0.8% particle volume fraction)	4.5	4.7

Matrix Young's modulus $E_m=4.6$ GPa and filler Young's modulus $E_f=70$ GPa.

the characterization of other mechanical properties such as the transverse moduli, shear moduli and Poisson's ratios or other physical properties such as the thermal and electrical conductivities.

6. Discussion

The developed multi-domain 3D BEM code has demonstrated to be very effective and accurate for material simulation involving thin films and complex configuration. These simulations could be prohibitively challenging for the domain-based FEM. However, there is still much to do before the developed BEM code can be applied to solve realistic material modeling problems that are likely to involve large scales and multiphysics.

The new developed BEM, which is based on the conventional BEM approach using direct solvers, can only handle models of a few thousand elements and is limited to composite models with only several tens of fibers or particles with a desktop computer. The efficiency of the BEM code needs to be improved with the fast multipole methods, which have demonstrated superior efficiency in solving large BEM models (with the DOF's above several millions) [34,35]. Indeed, very large BEM models of RVEs containing several thousands of fibers with the total DOF's above 10 millions have been solved successfully with the fast multipole accelerated BEM using a rigid-inclusion model and constant elements [36]. These large-scale models are necessary when the composites contain randomly distributed and oriented fillers that cannot be modeled accurately with small to moderate-scale RVE models. The current multi-domain BEM using quadratic elements and capable of computing all nearly-singular integrals accurately has paved the way for large-scale modeling of composites with even higher efficiency.

7. Conclusion

A robust 3D multi-domain BEM code, which can handle thin shapes in a domain and a large number of domains, has been developed for the study of composite materials. In this improved BEM implementation, a nonlinear coordinate

transformation is applied on the element of integration with the source point near by, in combination with the line integral approach. Significant improvements in the accuracy of evaluating nearly-singular integrals have been obtained even when the distance (between the source point and the surface of integration) to element length ratio approaches to 1×10^{-6} . This is sufficient to deal with any thin domains in the simulation of material problems efficiently without having to use many smaller elements. Convincing results of the BEM simulation for thin films and fiber-reinforced composites demonstrate that the developed BEM can be an effective tool in composite material modeling and simulation. The developed BEM can be further accelerated by the fast multipole method to tackle more challenging material problems, such as large-scale modeling of nano-fiber or nano-particle reinforced composites.

Acknowledgements

The authors thank the two anonymous reviews for their helpful comments on this manuscript.

Appendix. Analytical solution for a coated spherical shell under a pressure load

The analytical solution of a coated shell (Fig. A1) under an external pressure load is derived in this section. This solution has been used to verify the BEM results in Section 5.

The stress, strain and displacement in the domain of the coating (outer shell) can be expressed as follows by considering a spherical shell with outer and inner pressure loads [37]

$$\sigma_r = \frac{p_0 b^3 (r^3 - a^3) + p_i a^3 (b^3 - r^3)}{r^3 (a^3 - b^3)}, \quad (\text{A.1})$$

$$\sigma_\theta = \sigma_t = \frac{p_0 b^3 (2r^3 + a^3) - p_i a^3 (2r^3 + b^3)}{2r^3 (a^3 - b^3)}, \quad (\text{A.2})$$

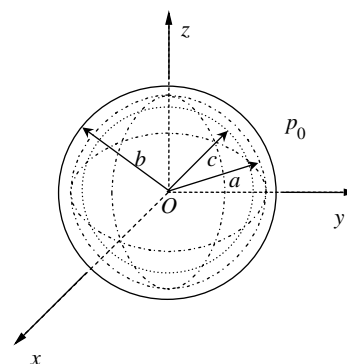


Fig. A1. A coated spherical shell (double shell) under external pressure p_0 .

$$\begin{aligned}\varepsilon_r &= \frac{\partial u}{\partial r} = \frac{1}{E_A} [\sigma_r - \nu_A(\sigma_\theta + \sigma_t)] \\ &= \frac{1}{E_A} \left[\frac{p_0 b^3 (r^3 - a^3) + p_i a^3 (b^3 - r^3)}{r^3 (a^3 - b^3)} \right. \\ &\quad \left. - \nu_A \frac{p_0 b^3 (2r^3 + a^3) - p_i a^3 (2r^3 + b^3)}{2r^3 (a^3 - b^3)} \right],\end{aligned}\quad (\text{A.3})$$

$$\begin{aligned}u_r &= \int \varepsilon_r dr = \int \frac{1}{E_A} \left[\frac{p_0 b^3 (r^3 - a^3) + p_i a^3 (b^3 - r^3)}{r^3 (a^3 - b^3)} \right. \\ &\quad \left. - \nu_A \frac{p_0 b^3 (2r^3 + a^3) - p_i a^3 (2r^3 + b^3)}{2r^3 (a^3 - b^3)} \right] dr \\ &= \frac{r(2\nu_A - 1)(p_i a^3 - p_0 b^3)}{E_A (a^3 - b^3)} + \frac{(1 + \nu_A) a^3 b^3 (p_0 - p_i)}{2E_A (a^3 - b^3) r^2},\end{aligned}\quad (\text{A.4})$$

where a and b are the radii of the interface and outer surfaces, respectively (Fig. A.1); r the distance from the origin to any point inside this domain ($a \leq r \leq b$); p_0 and p_i the external pressure and the normal pressure at interface, respectively; σ_r , σ_θ , ε_r and u_r the radial stress, hoop stress, radial strain and radial displacement, respectively; E_A and ν_A the Young's modulus and Poisson's ratio of the material, respectively.

The stress, strain and displacement in the inner spherical shell can be expressed as

$$\sigma_r = \frac{p_i a^3 (r^3 - c^3)}{r^3 (c^3 - a^3)}, \quad (\text{A.5})$$

$$\sigma_\theta = \sigma_t = \frac{p_i a^3 (2r^3 + c^3)}{2r^3 (c^3 - a^3)}, \quad (\text{A.6})$$

$$\begin{aligned}\varepsilon_r &= \frac{\partial u}{\partial r} = \frac{1}{E_B} [\sigma_r - \nu_B(\sigma_\theta + \sigma_t)] \\ &= \frac{1}{E_B} \left[\frac{p_i a^3 (r^3 - c^3)}{r^3 (c^3 - a^3)} - \nu_B \frac{p_i a^3 (2r^3 + c^3)}{2r^3 (c^3 - a^3)} \right],\end{aligned}\quad (\text{A.7})$$

$$\begin{aligned}u_r &= \int \varepsilon_r dr = \int \frac{1}{E_B} \left[\frac{p_i a^3 (r^3 - c^3)}{r^3 (c^3 - a^3)} - \nu_B \frac{p_i a^3 (2r^3 + c^3)}{2r^3 (c^3 - a^3)} \right] dr \\ &= \frac{r(2\nu_B - 1)(-p_i a^3)}{E_B (c^3 - a^3)} + \frac{(1 + \nu_B) c^3 a^3 p_i}{2E_B (c^3 - a^3) r^2},\end{aligned}\quad (\text{A.8})$$

where c is the radius of the inner surface, r the distance from the origin to any point inside this domain ($c \leq r \leq a$); E_B and ν_B the Young's modulus and Poisson's ratio of the material, respectively.

At the interface surface, where $r=a$, the radial displacement is calculated from the first domain by Eq. (A.4) is

$$u(a) = \frac{-3ab^3 p_0 (\nu_A - 1) + p_i [2a^4 (2\nu_A - 1) - ab^3 (1 + \nu_A)]}{2E_A (a^3 - b^3)}, \quad (\text{A.9})$$

and the radial displacement calculated from the second domain by Eq. (A.8) is:

$$u(a) = \frac{(2 - 4\nu_B) p_i a^4 + (1 + \nu_B) c^3 a p_i}{2E_B (c^3 - a^3)}, \quad (\text{A.10})$$

By equating Eqs. (A.9) and (A.10), we obtain the relationship between the external pressure p_0 and the interfacial pressure p_i as follows

$$p_i = \frac{3ab^3 (\nu_A - 1) p_0}{2E_A (a^3 - b^3) \left[\frac{-ab^3 (1 + \nu_A) + 2a^4 (2\nu_A - 1)}{2E_A (a^3 - b^3)} - \frac{2a^4 (2\nu_B - 1) - ac^3 (1 + \nu_B)}{2E_B (a^3 - c^3)} \right]}, \quad (\text{A.11})$$

By substituting Eq. (A.11) and the prescribed material properties into Eqs. (A.1)–(A.8), we can obtain the analytical solution for radial stress, hoop stress, radial strain and radial displacement at any point in the coated spherical shell.

References

- [1] Chen PE. Strength properties of discontinuous fiber composites. *Polym Eng Sci* 1971;11:51–6.
- [2] Goetler LA. Concise encyclopedia of composite materials. Oxford: Elsevier; 1994.
- [3] Zhu Y, Beyerlein JJ. Bone-shaped short fiber composites—an review. *Mater Sci Eng* 2002;A326:208–27.
- [4] Bhushan B. Tribology and mechanics of magnetic storage devices. New York: Springer; 1990.
- [5] Bhushan B. Mechanics and reliability of flexible magnetic media. New York: Springer; 1992.
- [6] Wood C, Perera A, Liu H, Broussard P, Adam J, Taylor DJ. Handbook of thin film devices. San Diego, CA: Academic Press; 2000.
- [7] Shan Z, Gokhale AM. Micromechanics of complex three-dimensional microstructures. *Acta Mater* 2001;49(11):2001–15.
- [8] Banerjee B, Cady CM, Adams DO. Micromechanics simulations of glass-estane mock polymer bonded explosives. *Model Simul Mater Sci Eng* 2003;11(4):457–75.
- [9] Pahr DH, Arnold SM. The applicability of the generalized method of cells for analyzing discontinuously reinforced composites. *Compos Part B Eng* 2002;33(2):153–70.
- [10] Xue M, Cheng L, Hu N. The stress analysis of sandwich shells faced with composite sheets based on 3D FEM. *Compos Struct* 2003;60(1):33–41.
- [11] Jensen KF, Rodgers ST, Venkataramani R. Multiscale modeling of thin film growth. *Curr Opin Solid State Mater Sci* 1998;3(6):562–9.
- [12] Mackerle J. Finite element and boundary element library for composites—a bibliography (1991–1993). *Finite Elem Anal Des* 1994;17:155–65.
- [13] Achenbach JD, Zhu H. Effect of interfacial zone on mechanical behavior and failure of fiber-reinforced composites. *J Mech Phys Solids* 1989;37(3):381–93.
- [14] Achenbach JD, Zhu H. Effect of interphases on micro and macromechanical behavior of hexagonal-array fiber composites. *J Appl Mech* 1990;57:956–63.
- [15] Liu YJ, Xu N, Luo JF. Modeling of interphases in fiber-reinforced composites under transverse loading using the boundary element method. *J Appl Mech* 2000;67(1):41–9.

- [16] Liu YJ, Xu N. Modeling of interface cracks in fiber-reinforced composites with the presence of interphases using the boundary element method. *Mech Mater* 2000;32(12):769–83.
- [17] Luo JF, Liu YJ, Berger EJ. Analysis of two-dimensional thin structures (from micro- to nano-scales) using the boundary element method. *Comput Mech* 1998;22:404–12.
- [18] Luo JF, Liu YJ, Berger EJ. Interfacial stress analysis for multi-coating systems using an advanced boundary element method. *Comput Mech* 2000;24(6):448–55.
- [19] Chen XL, Liu YJ. Thermal stress analysis of multi-layer thin films and coatings by an advanced boundary element method. *CMES: Comput Model Eng Sci* 2001;2(3):337–50.
- [20] Watson JO. Boundary elements from 1960 to the present day. *Electron J Boundary Elem* 2003;1(1):34–46.
- [21] Liu YJ, Rudolphi TJ. Some identities for fundamental solutions and their applications to weakly-singular boundary element formulations. *Eng Anal Boundary Elem* 1991;8(6):301–11.
- [22] Liu YJ, Rudolphi TJ. New identities for fundamental solutions and their applications to non-singular boundary element formulations. *Comput Mech* 1999;24(4):286–92.
- [23] Telles JCF. A self-adaptive co-ordinate transformation for efficient numerical evaluation of general boundary element integrals. *Int J Numer Methods Eng* 1987;24:959–73.
- [24] Nakagawa N. Near-surface field evaluation in two-phase Helmholtz problem. In: IABEM-93 symposium. August 16–19; 1993. Braunschweig.
- [25] Cruse TA, Aithal R. Non-singular boundary integral equation implementation. *Int J Numer Methods Eng* 1993;36:237–54.
- [26] Huang Q, Cruse TA. Some notes on singular integral techniques in boundary element analysis. *Int J Numer Methods Eng* 1993;36: 2643–59.
- [27] Liu YJ, Zhang DM, Rizzo FJ. Nearly singular and hypersingular integrals in the boundary element method. In: *Boundary elements XV*. Worcester, MA: Computational Mechanics Publications; 1993.
- [28] Liu YJ. Analysis of shell-like structures by the boundary element method based on 3-D elasticity: formulation and verification. *Int J Numer Methods Eng* 1998;41:541–58.
- [29] Mukherjee S, Chati MK, Shi XL. Evaluation of nearly singular integrals in boundary element contour and node methods for three-dimensional linear elasticity. *Int J Solids Struct* 2000;37(51): 7633–54.
- [30] Chen XL. Development of the boundary element method for the analysis of advanced materials. PhD Dissertation. Cincinnati: Mechanical Engineering Department, University of Cincinnati; 2004.
- [31] Hyer MW. Stress analysis of fiber-reinforced composite materials. 1st ed. Boston: McGraw-Hill; 1998.
- [32] Chen XL, Liu YJ. Square representative volume elements for evaluating the effective material properties of carbon nanotube-based composites. *Comput Mater Sci* 2004;29(1):1–11.
- [33] Ingber MS, Papathanasiou TD. A parallel-supercomputing investigation of the stiffness of aligned, short-fiber-reinforced composites using the boundary element method. *Int J Numer Methods Eng* 1997; 40:3477–91.
- [34] Nishimura N. Fast multipole accelerated boundary integral equation methods. *Appl Mech Rev* 2002;55:299–324.
- [35] Yoshida K, Nishimura N, Kobayashi S. Application of new fast multipole boundary integral equation method to crack problems in 3D. *Eng Anal Boundary Elem* 2001;25:239–47.
- [36] Liu YJ, Nishimura N, Otani Y, Takahashi T, Chen XL, Munakata H. A fast boundary element method for the analysis of fiber-reinforced composites based on a rigid-inclusion model. *ASME J Appl Mech* 2005;72(1):115–128.
- [37] Timoshenko SP, Goodier JN. *Theory of elasticity*. 3rd ed. New York: McGraw-Hill; 1987.